ELSEVIER

MPM/MD handshaking method for multiscale simulation and its application to high energy cluster impacts

Z. Guo, W. Yang*

Department of Engineering Mechanics, Tsinghua University, Beijing, 100084, China

Abstract

We propose a new multiscale simulation method which seamlessly combines the conventional molecular dynamics (MD) with the continuum mechanics formulated under the material point method (MPM). In MPM, modified interpolation shape functions are adopted to reduce artificial forces on the hierarchical background grids. The multiscale method is validated using the examples of step-like wave and wave packet propagations within a bar. The method is applicable to several kinds of potentials including the Lennard–Jones, EAM and a bonding-angle related potential for silicon. Examples of high energy Cu–Cu and Si–Si cluster impacts are presented. The evolution of displaced atoms is found to depend on the underlying lattice structures. For the case of Cu–Cu cluster impacts, stacking faults play an important role. The displaced atoms, visualized in the method of "local crystalline order", propagate in an anisotropic manner. This implies the anisotropy in energy transformation process through multi-interactions among cluster and surface atoms.
© 2005 Elsevier Ltd. All rights reserved.

Keywords: Multiscale simulation; Cluster impact; MPM/MD handshaking

1. Introduction

Many physical phenomena, such as crack propagation, turbulence, and high energy cluster impacts, occur in multiple length scales. Different length scales interact strongly to generate complicated behaviors. These phenomena pose notorious difficulty in computation. Although the continuing advances in massively parallel computing have reached the capacity of simulating as many as 19 billion atoms [1], it is not easy to model the mesoscale and macroscale events even with this formidable computational power. A frequent scenario is that a vast region of these phenomena does not require explicit atomistic treatment. To reduce the burden of computation, the combined atomistic and continuum description was developed to bridge various length scales [2–7]. Here we add to this practice by advocating a new multiscale scheme that seamlessly handshakes the conventional molecular dynamics (MD) and the material point method (MPM). In

this scheme, an atomistic region is surrounded with a MPM continuum region. Proper boundary conditions are developed between the two regions to ensure seamless coupling.

In the last decade, high energy cluster impacts have arose much interest in the thin film growth. A number of impact experiments and simulations have been reported [8–13], addressing various issues on aspects concerning the materials, the cluster size, the incident energy, the damage formation, the crater formation, and the sputtering technique. The process of high energy cluster impacts inherently involves complex and multidimensional deformations, produces high pressure, temperature and shock waves, and introduces melting or even evaporation [14,15]. Were these phenomena described by a continuum description, the conservation equation of energy, together with the conservation equations of mass and momentum, should be used to consider the thermal effects. To close the governing equations, an equation of state (EOS, a relationship among pressure, volume and internal energy) is also required. Yet simple EOS, such as the EOS of Tillotson [16], cannot accurately describe the intricate process. MD avoids a

---

*Corresponding author. Tel.: +86 10 62782642; fax: +86 10 62781824.
  E-mail address: yw-dem@tsinghua.edu.cn (W. Yang).

priori imposition of the EOS and requires only reliable potentials. Yet MD simulations are limited by the computation capacity addressed before. Therefore, the combined MD and continuum formulation is suitable to model these highly challenging phenomena.

During the process of energetic cluster impacts, atoms near the impingement site are seriously distorted to different kinds of structures, and they can even be squeezed to the very proximity with each other. Energized atoms can have much higher velocity, escape the bondage of the substrate and flee away as monomers and small clusters. The process manifests in the form of a melting crater. Thus a reliable potential should be employed [17] in the MD region to describe this highly distorted region. In the nearby region of the crater, atoms are seriously disturbed and produce highly nonlinear deformation. This region is also modeled with MD description. Leaving away from the impingement site, atoms still keep vibrating in small deformation near ideal lattice sites. We use MPM to handle this less entangled region. This macroscopic description merely needs proper constitutive relations for specific materials.

The plan of the paper is as follows: after an outline of MPM, the coupling of the multiscale method is described in detail. Tests are presented to demonstrate the satisfactory performance of the method. The method is then applied to energetic cluster impacts. The results will show that the underlying lattice structures play an important role in the process of impacts.

2. MPM/MD handshaking method

2.1. The material point method (MPM)

Motion of a continuum is governed by conservation equations of mass, momentum and energy. If one lets ρ be the mass density, v the velocity, σ the Cauchy stress, b the specific body force and a the acceleration, the conservation equations for mass and momentum are

$$\dot{\rho} = -\rho \nabla \cdot v, \tag{1}$$

$$\nabla \cdot \sigma + \rho b = \rho a. \tag{2}$$

Though not listed here, one has to bear in mind that the consideration of thermal effects may involve the conservation of energy. In MPM, a material is discretized into a collection of material points (particles) as illustrated in Fig. 1(a). Each material point is assigned a mass based on the volume it covers and the initial mass density. Eq. (1) is satisfied if the mass of each material point is kept fixed throughout the computation. To provide a Lagrangian description of material points, other properties, such as position, velocity, acceleration, stress, strain and constitutive parameters are also assigned to each material point. The Lagrangian scheme usually results in mesh lockup and entanglement if the material is seriously distorted. Yet in MPM the conservation equation of momentum is solved
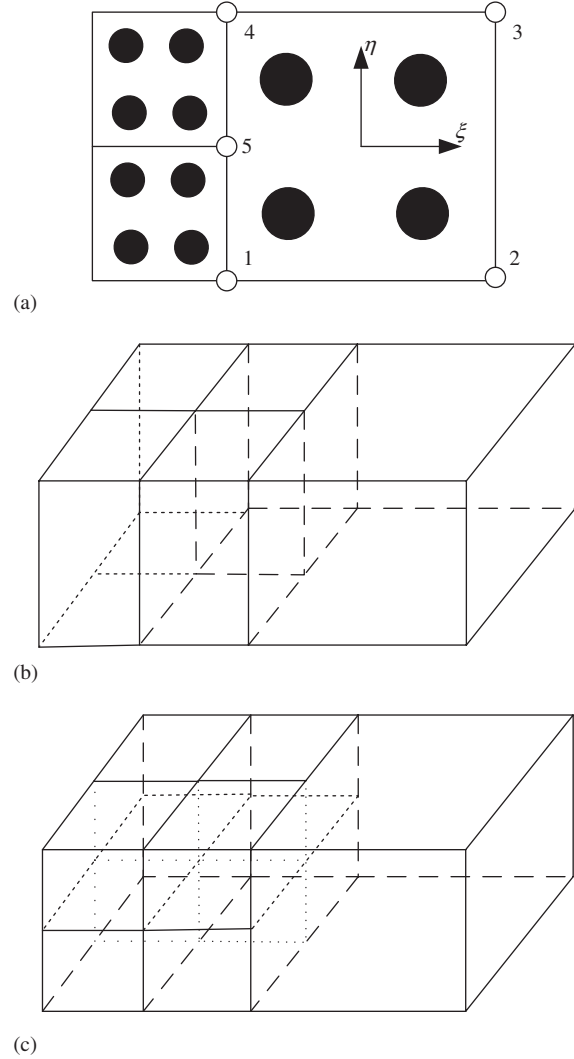

Fig. 1. (a) A schematic view of two-dimensional (2-D) MPM calculation. The solid lines show a regular hierarchical grid. The black dots are material points. Four material points in each element are located at the reduced coordinates ($\pm 0.5, \pm 0.5$) and this arrangement is usually adopted in MPM. Graphs (b) and (c) delineate two kinds of three-dimensional (3-D) hierarchical grids. Four and eight finer background elements are condensed to one big element.

on a background Eulerian mesh and thus avoids the trouble of mesh entanglement. For clarity, in this paper all variables with subscript i or j are associated with Eulerian description, representing values on background grids. Variables associated with Lagrangian description, representing material point values, are labeled by subscript p. The discretized form of Eq. (2) takes the following form [18]

$$\sum_{j=1}^{N_g} m_{ij} a_j = f_i^{\text{int}} + f_i^{\text{ext}}, \quad i = 1, \cdots, N_g, \tag{3}$$

where m_{ij} is the consistent mass matrix, a_j is the acceleration on node j, f_i^{int} and f_i^{ext} are the internal and external forces on node i, and N_g is the number of grid

nodes. By introducing interpolation shape functions, the mass matrix, internal and external forces are defined by [18]

$$m_{ij} = \sum_{p=1}^{N_p} m_p N_i(\boldsymbol{x_p}) N_j(\boldsymbol{x_p}), \qquad (4)$$

$$\boldsymbol{f}_i^{\text{int}} = \sum_{p=1}^{N_p} -V_p \sigma(\boldsymbol{x_p}) \cdot \nabla N_i(\boldsymbol{x_p}),$$

$$\boldsymbol{f}_i^{\text{ext}} = \hat{\boldsymbol{\tau}}_i + \sum_{p=1}^{N_p} m_p \boldsymbol{b}(\boldsymbol{x_p}) N_i(\boldsymbol{x_p}), \qquad (5)$$

where m_p and V_p are the mass and volume of the pth material point, $N_i(\boldsymbol{x})$ is the interpolation shape function on node i, $\hat{\boldsymbol{\tau}}_i$ is the surface traction associated with node i, and N_p is the number of material points. Usually the consistent mass matrix is replaced by a diagonal mass matrix for computation efficiency. The expense is a slight amount of numerical dissipation [19]. By doing so, Eq. (3) takes the reduced form

$$m_i \boldsymbol{a}_i = \boldsymbol{f}_i^{\text{int}} + \boldsymbol{f}_i^{\text{ext}}, \quad i = 1, \cdots, N_g, \qquad (6)$$

where the diagonal mass matrix is

$$m_i = \sum_{p=1}^{N_p} m_p N_i(\boldsymbol{x_p}), \quad i = 1, \cdots, N_g. \qquad (7)$$

The discrete momentum conservation equation (Eq. (6)) is solved on a background grid. The obtained grid accelerations are used to update the state of each material point. To update the stress state on each material point, a constitutive relation is required. The Lagrangian description of MPM follows with material points and thus easily accommodates a history dependant constitutive relation. In this paper, our attention is focused on the coupling of different regions, i.e. the MPM/MD regions. The coupling needs the match of constitutive relations in the two regions. Their difference in formulations dictates that the matching can only be enforced in the elastic regime when atoms or material points in the coupling layer are vibrating from their equilibrium sites in small amplitude. For linear elastic materials, the relation between the stress and strain in the MPM region can be simplified as

$$\dot{\boldsymbol{\sigma}} = \boldsymbol{C} : \dot{\boldsymbol{\varepsilon}}, \text{ where } \boldsymbol{\varepsilon} = \frac{1}{2} \left[(\nabla \boldsymbol{u}) + (\nabla \boldsymbol{u})^{\text{T}} \right]. \qquad (8)$$

The symbol $\boldsymbol{C}$ denotes the fourth-rank elasticity tensor and $\boldsymbol{u}$ the displacement field. For nonlinear elastic materials, $\boldsymbol{C}$ is a tangential stiffness tensor and varies with the strain of the material. After updating the information on material points, the background mesh can be discarded which enables adaptive meshing [20] or reused for the next time step. Details of time-integration algorithm can be found in Ref. [18]. Several kinds of modified algorithm [21,22] are employed to improve the accuracy. In this paper, we adopt the algorithm described in Ref. [21]. A fixed Eulerian background mesh is used here for simplicity.

For most MPM calculations, standard finite element (FE) shape functions [23] are adopted to map information between material points and background grids [20]. For the hierarchical grid as illustrated in Fig. 1(a), the standard FE shape function on node 5 is

$$N_5(\xi, \eta) = \frac{1}{2}(1 - \xi)(1 - \eta^2). \qquad (9)$$

Consider the special case of a uniformly stressed state, the internal force (Eq. (5)) simplifies to

$$\boldsymbol{f}_i^{\text{int}} = -\sigma \cdot \sum_{p=1}^{N_p} V_p \nabla N_i(\boldsymbol{x_p}), \text{ where } \sigma = \sigma(\boldsymbol{x_p}) \forall p. \qquad (10)$$

For the hierarchical grid in Fig. 1(a), $\boldsymbol{f}_i^{\text{int}}$ is not zero (for $i = 1$, 4 and 5). We call this non-zero $\boldsymbol{f}_i^{\text{int}}$ the artificial forces. To suppress its occurrence, we modify the interpolation shape functions. The square terms in the standard FE shape functions are replaced with their absolute value. For example, the interpolation shape function on node 5 in Fig. 1(a) is modified to the following bilinear form

$$N_5(\xi, \eta) = \frac{1}{2}(1 - \xi)(1 - |\eta|). \qquad (11)$$

Similar modification can be exercised for three-dimensional (3-D) background grids, i.e. replacing the square terms with their absolute value. By doing so, the internal forces vanish for the special case in Fig. 1(a). It is also true for the 3-D cases as illustrated in Fig. 1(b) and (c) if eight material points are located at the reduced coordinates $(\pm 0.5, \pm 0.5, \pm 0.5)$. After modification, the interpolation shape functions are linear in each direction, so that the modification can suppress artificial forces on hierarchical nodes. A step stress wave is used to test the modified interpolation shape functions in hierarchical MPM scheme. The stress wave propagates along $[\bar{1}\,0\,0]$ direction. Sliding boundary conditions are employed in directions perpendicular to $[1\,0\,0]$. The 3-D background mesh in Fig. 1(c) is employed and each contains eight material points, that are initially located at the reduced coordinates $(\pm 0.5, \pm 0.5, \pm 0.5)$. Fig. 2 shows the snapshots of the stress wave propagating along $[\bar{1}\,0\,0]$. It can be seen that along the boundary of hierarchical background grids there are no visible artificial forces. The simulated stress wave agrees well with the analytical stress wave. It can also be seen that some small short-wavelength phonons are not supported by the coarse MPM region and part of the stress wave is reflected on the boundary. Proper damping [24] on the boundary is expected to reduce the amplitude of the reflected waves.

One drawback of the linear interpolation shape functions is that the functions are not smooth across adjacent cells. The lack of smoothness can produce numerical noise in MPM. The generalized interpolation MPM [25] can remove numerical artifacts inherent in the MPM formulation when material points fail to register in a self-similar fashion on the background computational grid. To focus
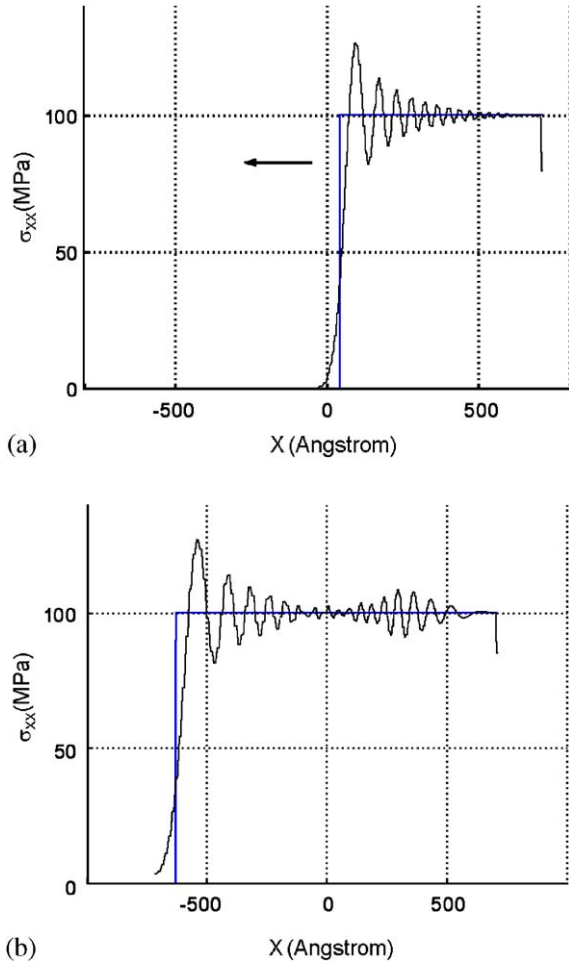
Fig. 2. Amplitude of a step stress wave propagating from a finer MPM region to a coarser MPM region. The two regions are separated by $x = 0$. The step line is the corresponding analytical stress wave with amplitude of 100 MPa. (a) Profile of the stress wave in the MPM finer region. (b) Profile of the stress wave that has passed into the coarser MPM region.

our attention on the coupling of the MPM/MD regions, we instead use the linearized interpolation shape functions proposed here.

2.2. The handshaking of MPM/MD regions

Embedded-atom method (EAM) potentials [26] provide a simple framework for accurate description of noble transition metals. In EAM scheme, the total energy of a mono-atomic system is represented as

$$E_{\text{tot}} = \frac{1}{2}\sum_{ij}\phi(r_{ij}) + \sum_i F(\bar{\rho}_i). \qquad (12)$$

Here $\phi(r_{ij})$ is a pair potential as a function of distance between atoms i and j, and F is the embedding energy as a function of the host electron density $\bar{\rho}_i$ at site i which is induced by the other atoms in the system as

$$\bar{\rho}_i = \sum_{j \neq i}\rho(r_{ij}). \qquad (13)$$

Here $\rho(r_{ij})$ is the electron density function. The second term in Eq. (12) is volume dependent and represents, in an approximate manner, many-body interactions in the system. Thus many-body effects are facilely considered by introducing the embedding energy function, and the computation efficiency is comparable to simple pair potential models. Because EAM potentials are widely used in MD simulations, we choose them to illustrate the coupling of MPM/MD regions. The successful inclusion of the many-body effects would render its application to pair and triple potentials straightforward.

The handshaking scheme described here spatially divides the physical system into the MPM/MD regions (Fig. 3). An imaginary surface (interface) is drawn between the MPM and MD regions. The handshaking domain is composed of regions I, II and III. The width of each region should be not less than a potential cutoff. In regions II and III, material points are initially located at the ideal lattice sites. Displacement boundary conditions are employed to decouple the two regions [2]. Regions II and III supply the boundary conditions for the MD region as illustrated in the top diagram in Fig. 3 (b). Conversely, as illustrated in the bottom diagram in Fig. 3(b) atoms in region I supply the boundary conditions for the MPM continuum region. At each time step in the MD calculation, particles in regions II and III are viewed as atoms (Fig. 3 (b)). Position of each atom in regions II and III is conveyed from the position of the corresponding particle. Forces on each atom in the MD region are obtained from the total energy (Eq. (12)) by taking derivatives with respect to the atomic coordinates. Particles in regions II and III have different bearings in the MD and the continuum calculations. In the MD calculation, each particle is assigned an electron cloud density under Eq. (13). The electron density on each particle in region II is partly induced by particles in region III so that the latter serves to provide an atomic atmosphere to particles in region II. Similarly, the electron density on each atom in region I is partly induced by particles in region II, and region II serves to provide an atomic atmosphere to atoms in region I. Accordingly, an electron density corresponding to the deformation throughout the simulation is correctly obtained in regions I and II. At each time step in the MPM calculation, atoms in region I are viewed as particles (Fig. 3 (b)), and each particle receive information, such as mass, volume, position, velocity and stress that needed for MPM calculations, from the corresponding atoms. The background mesh is extended to region I for the MPM calculation. Each particle evolves under the discrete momentum equation (Eq. (6)). In the MPM calculation, atoms in region I are different from the atoms in the MD calculation. They evolve under the discrete momentum equation which is solved on background grids. Thus the mass, velocity and internal force on the background grids near the MPM/MD interface are partly induced from the "particles" in region I.
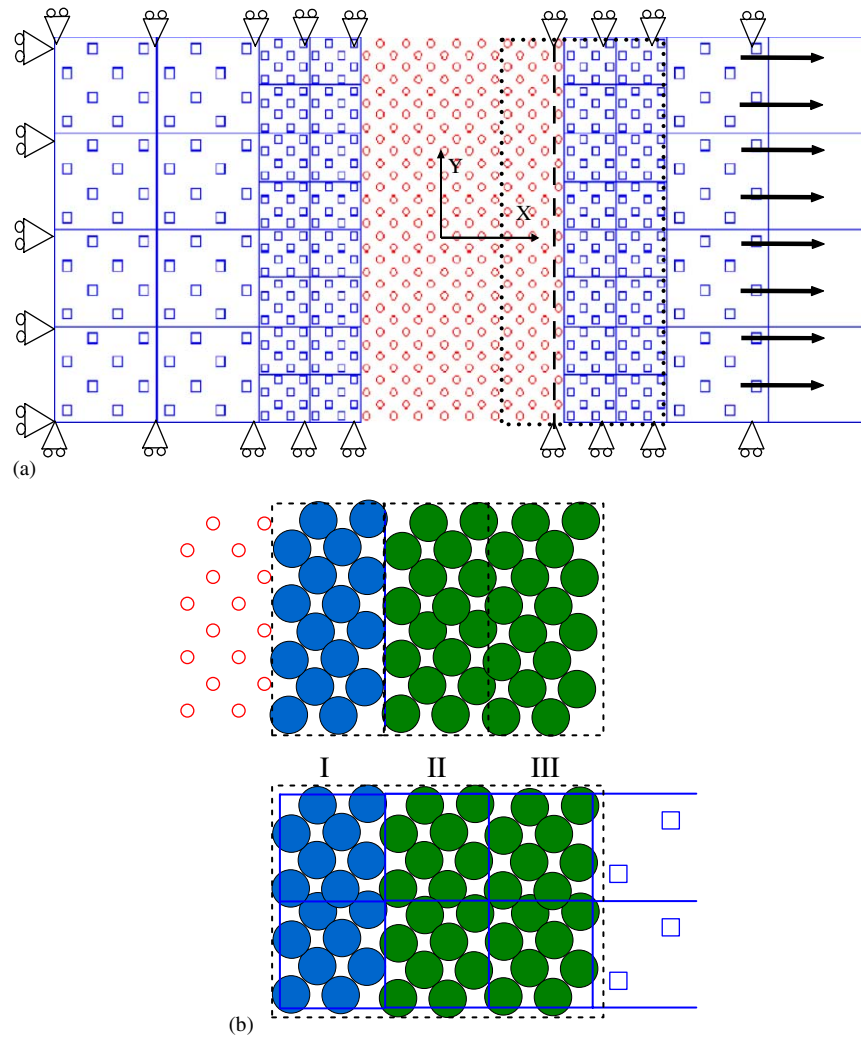
Fig. 3. (a) Schematic view of a bar under tension. Only a slice of the bar (FCC crystal) is shown. Big squares represent heavy material points. Small squares represent light material points. Circles represent atoms. The solid lines delineate the background mesh. Dotted boxes denote the right part of the handshaking region. The dashed line represents the interface between the MPM and MD regions. Right arrows symbolize boundary forces under 500 MPa theoretical stress. Graph (b) enlarges the handshaking region in (a). Filled circles in region I represent atoms. Filled circles in regions II and III are material points. The top diagram in (b) elucidates the MD calculations and the bottom one the MPM calculations. Background mesh is extended to region I for MPM calculations.

After the two regions decouple as illustrated in Fig. 3 (b), each region evolves under their governing equations concurrently with a suitable time step. For MPM, the critical time step is proportional to the smallest element size and inversely proportional to the wave speed of the material [27]. In the MPM/MD handshaking scheme proposed here, the concurrent time step, determined by the time step for the MD calculation, is in the magnitude of fs and is small enough for the stability of MPM calculations.

The decouple scheme ensures equality of the displacement field in the MD/MPM regions. Since forces are explicitly avoided in the decouple scheme, the stress equilibrium between the two regions is not established a priori. As pointed out by Kohlhoff et al. in Ref. [2], the stress equilibrium in the two regions requires the equal elastic constants between the continuum/MD regions. Also

it can be seen in the validation part that the matching of elastic constants in the MD/MPM regions is a necessary condition. For simplicity, up to second-order elastic constants are considered here, which corresponding to linear elasticity. For cubic crystals under linear deformation, there are three elastic constants C_{11}, C_{12} and C_{44}. These constants can be derived from the atomic potential and then are used in the MPM region. Thus the MPM region only sustains elastic deformation. The dividing of the MD/MPM regions should be based on physical conditions. When plastic deformation approaches the handshaking region, the MD region should be extended to ensure the covering of the inelastic region throughout the simulation. Also when there is no need of MD description, that region should be reversed into the MPM region. The hierarchical, adaptive, material point method developed by Tan and Nairn [20] is expected to achieve this

goal. Here in our simulation the MD region is large enough and the MPM region only sustains linear elastic deformation. Thus a fixed background mesh is adopted for simplicity.

Leaving the handshaking region, material points are enlarged to represent many atoms, rendering the computational efficiency of MPM. We generalize the hierarchical background mesh [20] to the 3-D case. For bulk materials, the background mesh can be enlarged in three directions, i.e. eight elements condense to one big element (Fig. 1(c)). Similarly for plates and bars, the background mesh can be enlarged in two (Fig. 1(b)) or one directions, i.e. four or two elements condense to one element. Material points are enlarged in proportion to the background mesh. The mass of each material point is proportional to the volume it covers. The coarser the mesh, the heavier the material points initially placed in that element. The reduced coordination of each material point is the same after the enlargement, i.e. the material points and background mesh are enlarged proportionally. The enlargement results in missing degrees of freedom. As the size of background mesh increases, a small portion of short-wavelength phonons are not supported by the coarser mesh, as shown in Fig. 2. The largest spacing depends on the shortest wavelength phonons expected to propagate unimpeded in the MPM region.

2.3. Validation of the MPM/MD handshaking method

The multiscale method developed here handshakes the MD/MPM regions. The MPM region provides an environment for the MD region. The seamlessness of the method has two meanings. First, the outer load applied in the MPM region can pass into the MD region without obvious hindering. Second, the disturbance in the MD region, arising from the bond breaking at the crack tip [4] or from energetic cluster impacts, can propagate into the MPM region without obvious reflection. Usually the former is easy to be implemented, while the latter is more difficult to be achieved since the continuum region usually is coarser and may not support some short-wavelength phonons. Thus the validation here is divided into two parts, validating the two meanings separately.

The first example tests the transmission ability from the MPM region to the MD region. An undisturbed FCC crystal lattice was embedded in the MPM region as illustrated in Fig. 3(a). The bar is 3-D but only a slice of which is shown. A uniform tensile step force is applied at time zero at the right end of the bar. Hierarchical mesh (of rather large mesh size) and material points are employed in the MPM region. In the handshaking region material points are placed at the ideal crystal lattice sites. In the coarse MPM region, eight finer elements and lighter material points condense to one big element and one heavier material point (Fig. 1(c)). Forces on boundary are applied on material points along [1 0 0]. In Y, Z and $-X$ directions we use sliding boundary conditions. Periodic

side boundary conditions are applied in the MD region for the consistency with the MPM region. The potential in Ref. [28] for Cu is employed here. The initial temperature is set at zero. The definition of the stress on an atom is based on Virial theorem. Here we use the stress used by Schiøtz et al. [29]. Note that the bar in Fig. 3(a) is only a schematic view and the true region of simulation is much larger.

Fig. 4 shows the passing of stress wave from the MPM to the MD region. The analytical solution is obtained by using the elastic constants in the MPM region. It can be seen that the simulation results agree well with the analytical solution. No visible wave reflection is observed in the handshaking region. Note that the stress configuration fluctuates along the analytical solution. The fluctuation in the MPM region is partly due to discretization since a continuum of infinite degrees of freedom is replaced by material points of limited degrees of freedom. Another reason is the lack of smoothness of the interpolation shape functions. The generalized interpolation MPM [25] can reduce numerical artifact noise which might be expected in MPM calculations. Contrasting with that in MPM region, the fluctuation in MD region is intrinsic since atoms are discrete.

For the purposes of comparison, we also show the results when the elastic constant C_{11} in the MPM region are twice as large as that of the MD region (Fig. 5). For this case, the simulated wave velocity and profile deviate significantly from their analytical counterparts. The analytical wave moves fast because the elastic constant C_{11} in the MPM region is larger. The stress in the MD region is lower due to the smaller deformation in the stiffer MPM region. Figs. 4 and 5 indicate that σ_{xx} is continuous in the handshaking region, which is expected from the continuum stress wave theory. The lateral stress components σ_{yy} and σ_{zz}, on the other hand, may suffer jumps across the interface if elastic constants on the two sides mismatch each other. To validate the seamlessness of this method, one needs to
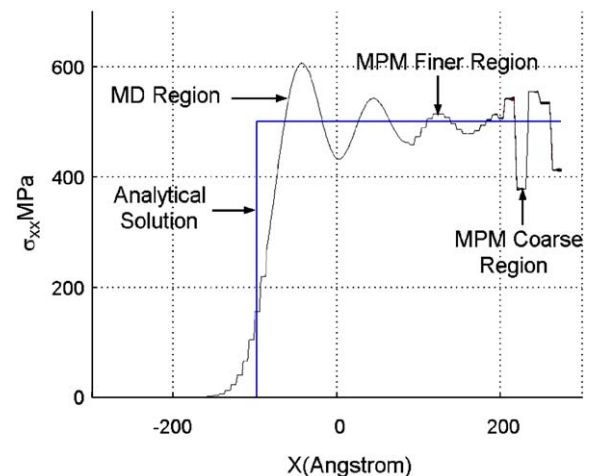

Fig. 4. Stress wave propagates from the MPM region to the MD region. The analytical solution corresponds to a 500 MPa step stress wave. Different regions are denoted in the figure.
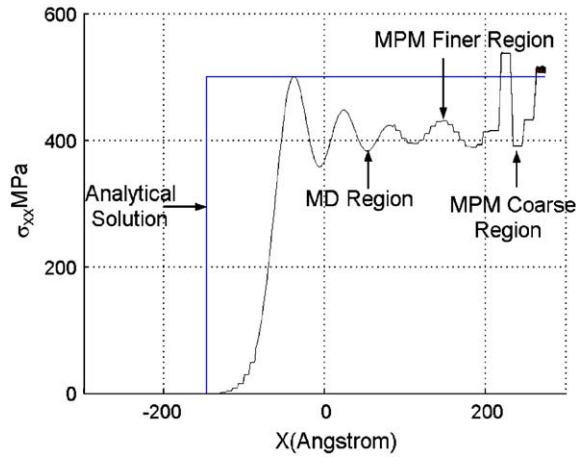
Fig. 5. Stress wave profile when C_{11} in MPM region is twice of that in the MD region.
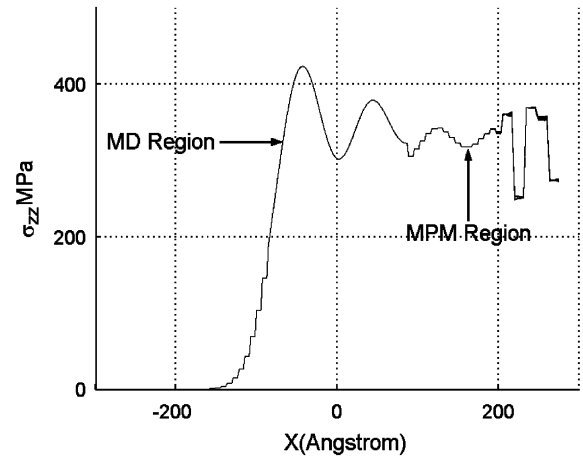

Fig. 7. Profile of the lateral stress component σ_{zz} along the bar for the case of elastic constants on the MPM/MD regions match each other.
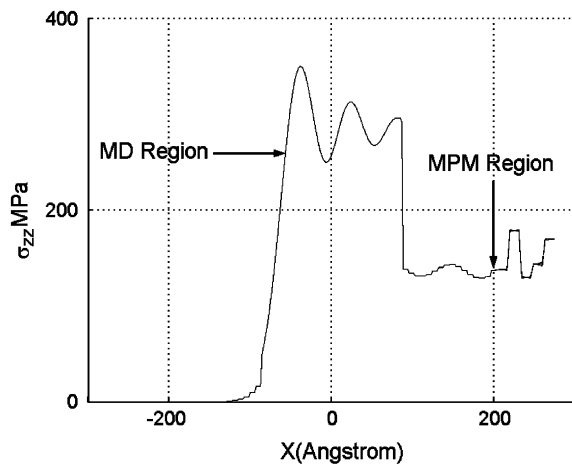

Fig. 6. Profile of the stress component σ_{zz} along the bar. In this case the elastic constant C_{11} in the MPM region is twice of that in the MD region.
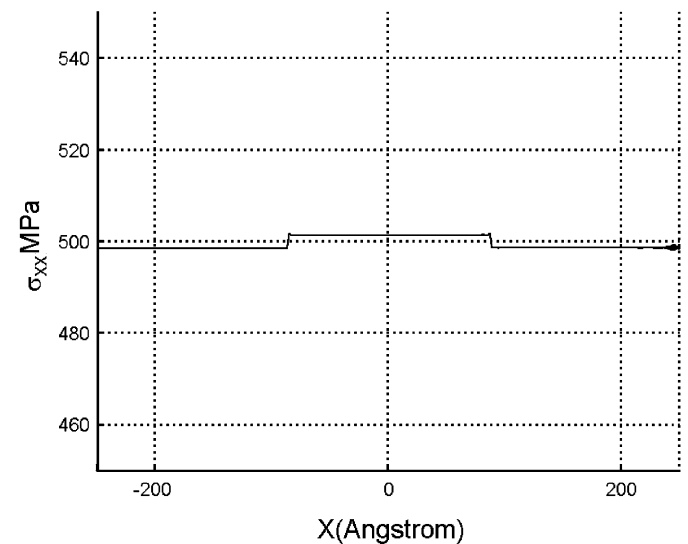

Fig. 8. Profile of the lateral stress component σ_{xx} along the bar for static loading.

make sure that the lateral stresses are also continuous on the two sides. Fig. 6 shows the profile of σ_{zz} along the bar for the case when elastic constants on the two sides are mismatched. A big jump occurs across the MPM/MD interface. Fig. 7 shows the profile of σ_{zz} along the bar for the case of elastic constants on the MPM/MD regions that match each other. The equal level of σ_{zz} on two sides of the interface indicates that this MPM/MD handshaking scheme looks seamless.

The quasi-static performance of this MPM/MD handshaking method is also tested. A damping force is used to quiet the bar. At long times, all velocities of material points and atoms approach zero and the final solution corresponds to a static loading of an end-loaded bar. The stress distribution is shown in Fig. 8. The distribution of σ_{xx} is not shown on the right MPM force boundary since solutions are usually not very accurate on the boundary just like FE method. The stress in the MD region is slightly higher and the stress in the MPM region is slightly lower.

The maximum deviation amounts to 0.36% of the true value, a scatter regarded acceptable for applications.

We also test the method for Lennard–Jones potential, EAM potential for BCC crystals [28] and a highly optimized empirical potential for silicon [30]. The results are similar and thus encouraging. From above one can see that the load applied in the MPM region can pass into the MD region almost without impeding.

Like Moseler et al. [24], we use Gaussian wave packets with small standard deviations to test the transmission ability of short-wavelength fluctuations produced in the MD region. The simulation configuration is similar with the configuration in Fig. 3, but the background mesh is uniform and refined, providing each particle occupies a mesh. The disturbance is first initiated in the MD region. Two Gaussian wave packets, with a standard deviation of one and a half lattice constant of copper, are initiated in
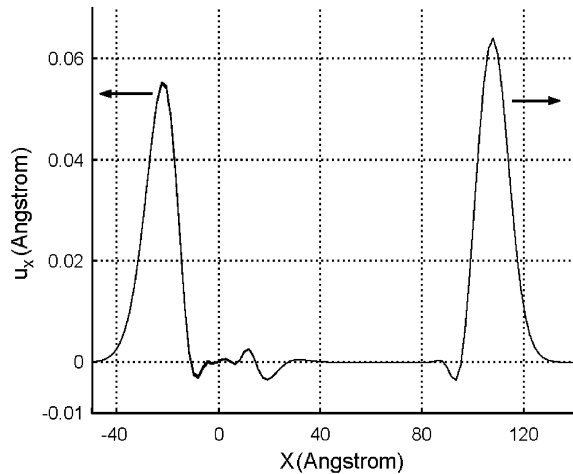
Fig. 9. Amplitude of two Gaussian wave packets. The region of $x > 0$ is the MD region. The region of $x < 0$ is the MPM region.
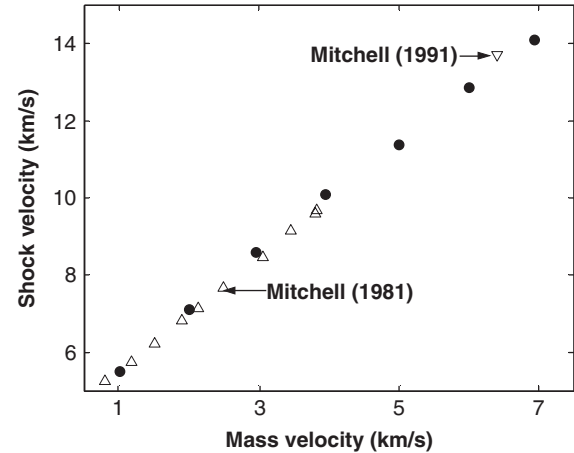

Fig. 10. The relationship between the mass velocity and the shock velocity. Filled circles are the simulation results using the EAM potential in Ref. [17]. Up and down triangles are experimental data of Mitchell et al. [32].

the MD region and they propagate in the opposite directions (Fig. 9). The leftward propagating wave passes from the MD region to the MPM region, while the rightward propagating wave is a reference and propagates always in the MD region. It can be seen that only a small fraction of wave is reflected back into the MD region. Even when the standard deviation is as small as one lattice constant, more than half of the energy passes into the MPM region. Moseler et al. found that a proper damping on the P–Q boundary could drastically reduce the amplitude of the reflected waves on the P–Q boundary [24]. Here damping is not employed in the handshaking region but the transmission ability is still better than the conventional Langevin MD [31] for Gaussian wave packets with standard deviation greater than one lattice constant.

3. Application to high energy cluster impacts

3.1. Evaluation of the EAM potential adopted in high energy cluster impacts

In high energy cluster impacts, atoms near the impingement site are distorted to different kinds of structures and they can be at the very proximity of each other. Thus a reliable potential should describe correct energy levels, configuration stability and atomic interactions at short separations. We choose the EAM potential proposed in Ref. [17]. The potential is fitted by using more fitting parameters and can accurately predict energies and stability of different coordination numbers. It is suitable for modeling surface sputtering and shock waves, and thus suitable for energetic cluster impacts.

We model the impact of two bars to evaluate the performance of the EAM potential developed by Mishin et al. [17]. The two bars are made of the same material, Copper. One bar flies with a certain velocity impacting with the other which is initially at rest. The initial temperature is set as 300 K. Periodic boundary conditions are employed

along directions perpendicular to the bar. After impact, two shock waves propagate from the impact interface into the interiors of bars. For symmetric impact (the flying object and the target is of the same material), the mass velocity (velocity of particles behind the shock front) is one half of the impact velocity according to the continuum theory. We find that the velocity of atoms behind the shock front oscillates around a certain value and can be far away from that value. But the averaged value of atoms behind the shock front is almost one half of the impact velocity. The mass velocity here denotes the averaged value. The shock velocity is the velocity of the shock front. Fig. 10 shows the relationship of the mass velocity and the shock velocity. It can be seen that simulation results agree well with the experiment data in Ref. [32] when the impact velocity is below 14 km/s (corresponding to a mass velocity of 7 km/s).

Fig. 11 shows the 293K isothermal pressure–volume relationship of the EAM potential in Ref. [17]. The results agree well with the experiment data in Ref. [33] at low pressure and at high pressure up to 1 TPa, they also agree with the first-principle calculations in Refs. [34,35].

3.2. Methodology of high energy cluster impacts

We use the multiscale simulation method proposed here to model high energy cluster impacts. Normal impacts of Cu clusters flying with a velocity of 10 km/s are simulated. The configuration (illustrated in Fig. 12) is arranged as follows. Cu clusters are formed from a spherical cutoff of an FCC lattice and are initially placed symmetrically above the target surface. The top surface (0 0 1) of the single crystal substrate is kept free and the rest five surfaces are fixed throughout the simulation. The time step is chosen to ensure that the changing of atom positions at one step is at least one magnitude smaller than the equilibrium atom spacing. The temperature is initially set at zero but allowed to evolve freely. For all cases the simulation time is up to

10 ps and the simulation region is chosen large enough to avoid the reflected waves from the fixed boundary to the MD region. For computational efficiency, the background mesh is not the finest. The background mesh in Fig. 12 can let a Gaussian wave packet with a standard deviation greater than three times lattice constant transmit the handshaking region without considerable reflection. For the impact of a cluster with 1052 atoms, the target is represented by a bulk region of dimension $277.6 \times 277.6 \times 138.8 \, nm^3$, containing over 2.3 million atoms and 0.5 million material points. Were the total region modeled with atomistic description, about 900 million atoms would

be needed. Material points are arranged in five hierarchical layers, with each material point in the outside layer condensates eight material points (binary condensation in each direction) in the inner layer.

The visualization of impacted atomistic system requires the identification of displaced atoms. A displaced atom is conventionally defined as an atom whose potential energy is a certain value above its bulk status [36]. This definition is followed in Refs. [10–12]. The certain arbitrariness of "a certain value" in that definition renders our adoption of another criterion. We define a displaced atom as an atom whose structure, in terms of the "local crystalline order" [37,38], is altered to a non-FCC structure. Different colors are assigned to different structures to provide a clear image of defects: atoms with local FCC order are referred to as a perfect lattice and are colored transparent, atoms on and above target surface are colored white denoting surface and sputtering atoms, atoms with local HCP order are colored red and thus denoting stacking faults, atoms with other 12-coordinated combinations are colored green, and atoms with none 12-coordinated combinations are colored yellow. For Si, displaced atoms are defined as those with none four-coordinated atoms and are colored green. Surface atoms are also colored white.

3.3. Simulation results

Graphs in Figs. 13–15 give snapshots of impact for clusters with 14, 128, and 1052 atoms. It can be seen that damage first spreads out almost in an isotropic manner (graph (a) of Figs. 13–15). Afterward, disordered atoms prefer to propagate along the four directions $[1\,0\,\bar{1}]$, $[\bar{1}\,0\,\bar{1}]$, $[0\,1\,\bar{1}]$ and $[0\,\bar{1}\,\bar{1}]$ (graphs (b) and (c) of Figs. 13–15). This
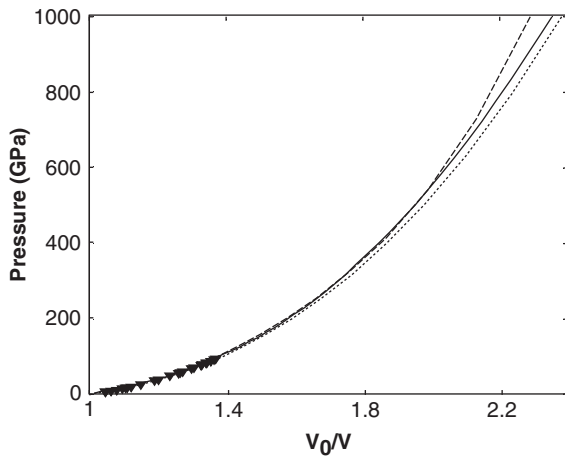

Fig. 11. 293 K isotherms for Cu. The solid line represents the simulation results using the EAM potential in Ref. [17], the downward pointing triangles are from Mao et al. [33], the dot line shows the calculated curve of Wang et al. [34], and the dashed line shows the calculated 300 K isotherms curve of Nellis et al. [35].
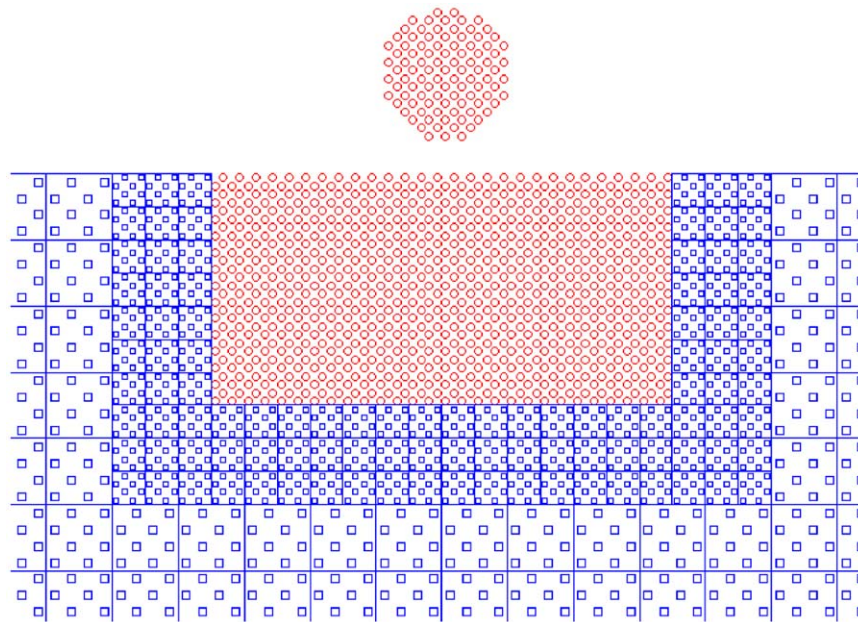

Fig. 12. A schematic view of high energy cluster impacts. Only a slice of material points and atoms are shown. Circles represent atoms. Small squares represent light material points, and big squares represent heavier material points. Solid lines denote the background mesh. Only one layer hierarchical grids are shown.
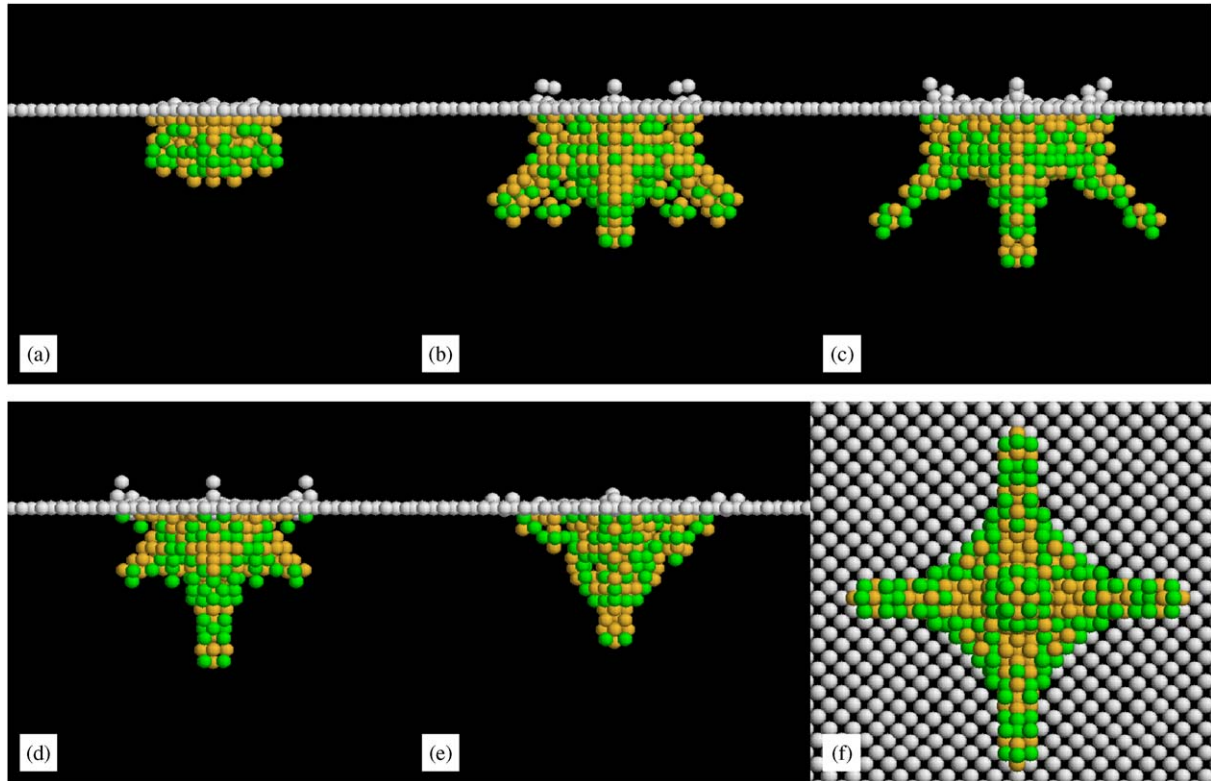
Fig. 13. (a)–(e) Frontal views (view from [1 0 0]) of local crystalline orders for 0.2, 0.4, 0.5, 0.7 and 1.0 ps after impact for the cluster with 14 atoms. Graph (f) shows the bottom view for graph (c). Only atoms with non-FCC crystalline order are shown.
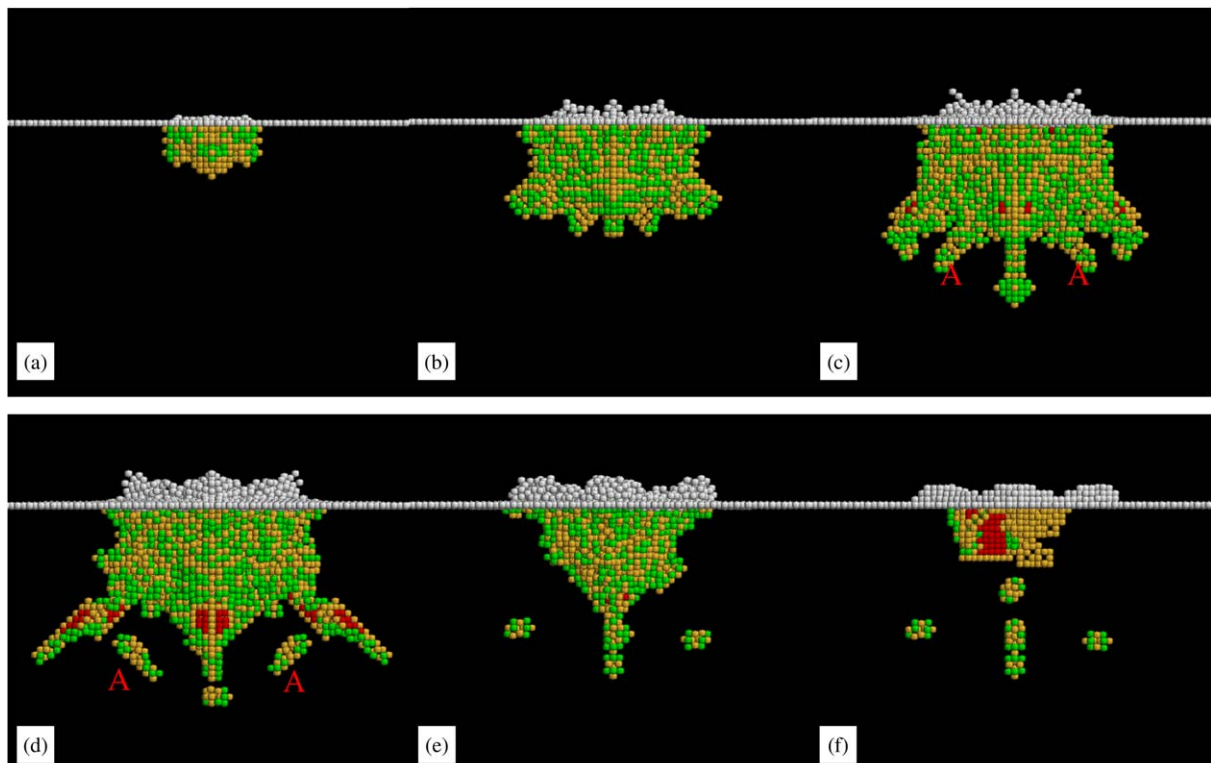

Fig. 14. (a)–(f) Frontal views of local crystalline orders for 0.2, 0.4, 0.7, 1.2, 3.1 and 10 ps after impact for the cluster with 128 atoms.
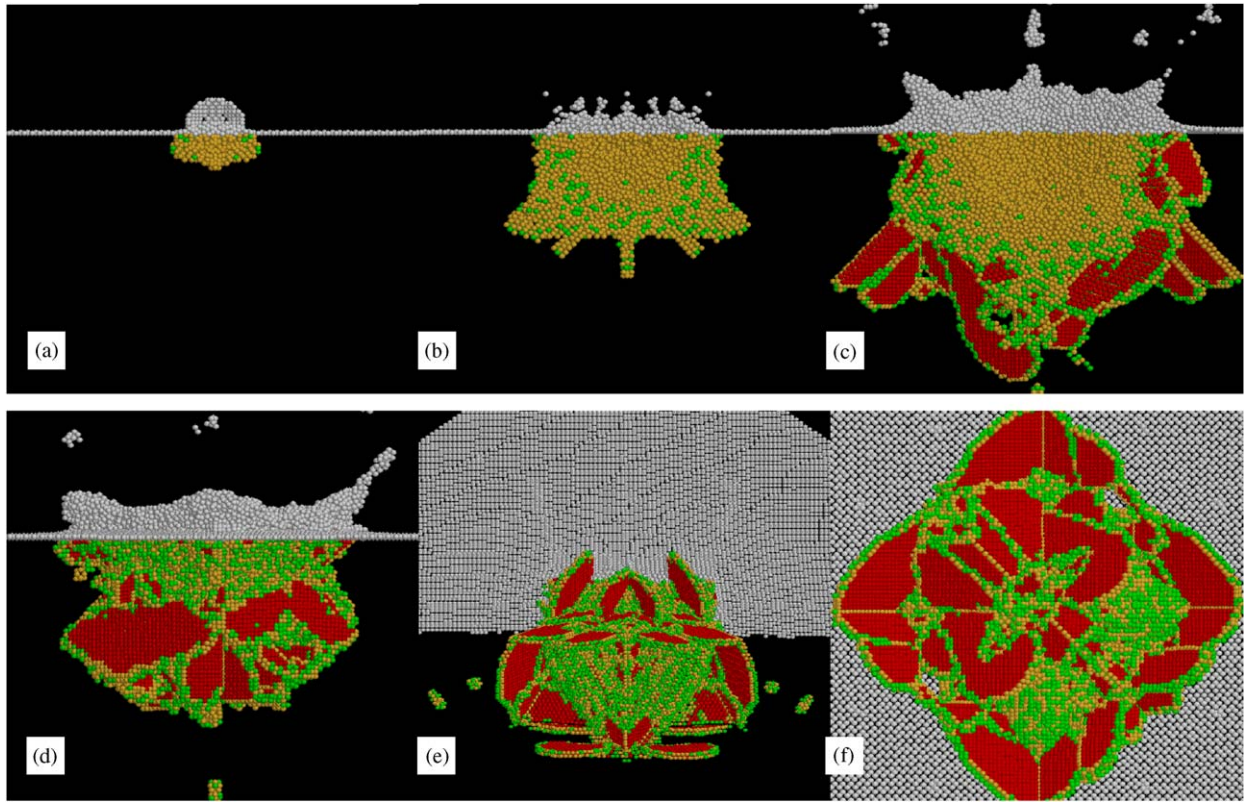
Fig. 15. (a)–(d) Frontal views of local crystalline orders for 0.2, 0.6, 4.2 and 6.2 ps after impact for the cluster with 1052 atoms. For clarity, the frontal half atoms of (b, c) are removed. Graph (e) is the view from [−1 1 −1] of graph (c), and graph (f) is the bottom view of graph (c).
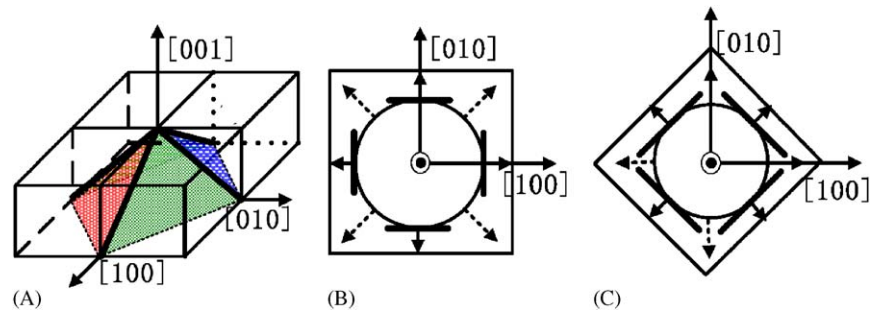

Fig. 16. Illustration of the deformation process. (A) Thick black lines denote the four intersection lines of four slip planes {1 1 1}. Damage prefers to propagate along the four thick black lines. Graphs (B) and (C), corresponding to the cases of small and large cluster impacts, respectively, show the deformation rate in different directions of the crater's top view. Thick back lines denote the planes that propagate in the directions shown by short solid arrows. This propagation leads to higher deformation rates in the directions of dotted long arrows.

damage evolution process is made clearer through the bottom view in Fig. 13(f). These four directions are denoted in Fig. 16(A) as thick black lines. Damage spread along the four intersection lines of the four closely packed slip planes {1 1 1}. As rarefaction waves come from the surface, the number of disordered atoms diminishes (Figs. 13(d–e), 14(d–f) and 15(d)). For the cluster with 14 atoms, hardly any disordered atoms are left after several picoseconds. For the cluster with 128 atoms, rarefaction waves let the disordered atoms labeled by "A" rotate inward, as shown in Fig. 14(c–d). Stacking faults appeared

in the later stage of impact and at 10 ps two partial dislocations interact with each other as shown in Fig. 14(f). For the cluster with 1052 atoms, the anisotropy is not evident compared with the clusters having fewer atoms. In the late stage of impact, many stacking faults appeared. The stacking faults propagate along the four close packed planes {1 1 1}. Most of them intersect on the four directions [1 0 $\bar{1}$], [$\bar{1}$ 0 $\bar{1}$], [0 1 $\bar{1}$], [0 $\bar{1}$ $\bar{1}$], and the rest on the two directions [1 1 0] and [1 $\bar{1}$ 0] (Fig. 15(c–f)). Dislocation loops can be observed in Fig. 15(c). It can also be seen that the four common slip directions of slip planes (illustrated in
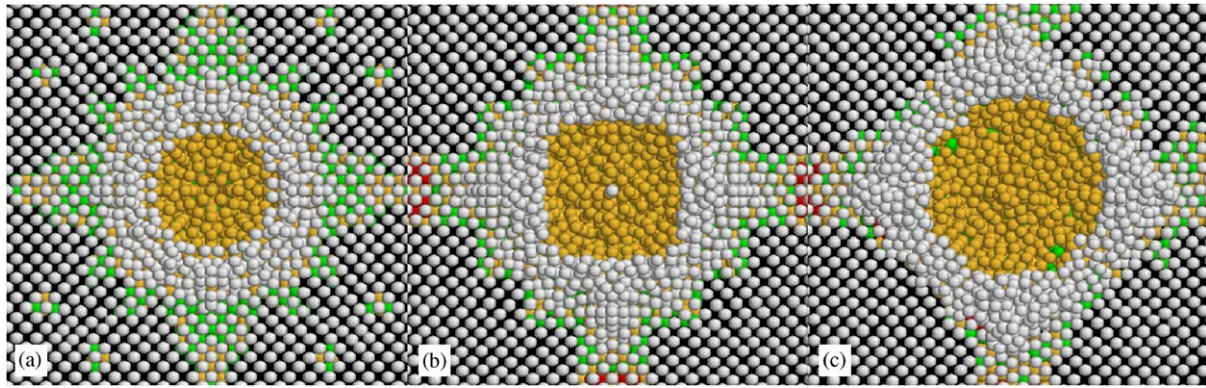
Fig. 17. (a)–(c) Top view of the local crystalline orders for 0.5, 0.8, 1.7 ps after the impact with a cluster of 128 atoms.
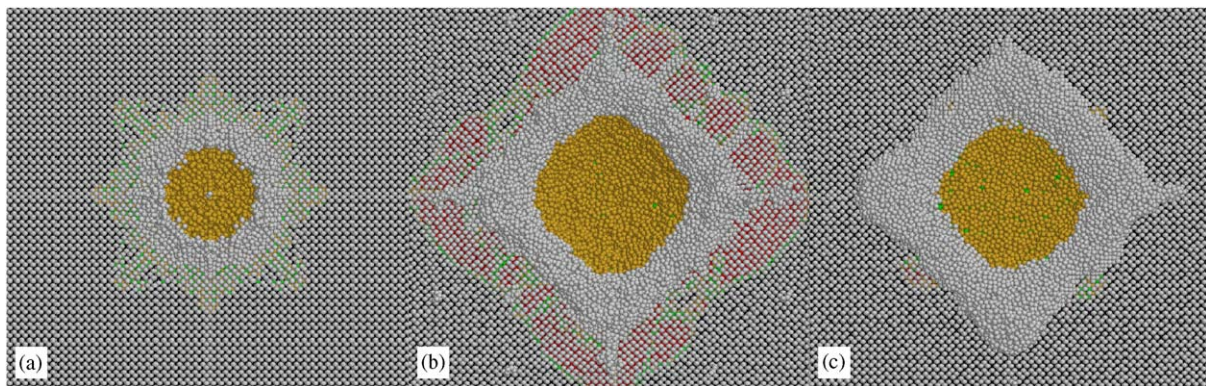

Fig. 18. (a)–(c) Top view of the local crystalline orders for 0.6, 4.2 and 10 ps after the impact with a cluster of 1052 atoms.

Fig. 16(A)) are the most favorable propagation paths of displaced atoms. For clusters with 14 and 128 atoms, hardly any sputtering yield is observed; while many monomers and small clusters are sputtered out for the cluster with 1052 atoms.

The evolution of crater shapes also indicates that the FCC lattice structure plays an important role in the impact process. For the cluster containing as few as 14 atoms, no observable crater is left after 10 ps. For the cluster with 128 atoms, the crater's top view evolves from a circle (Fig. 17(a)) to a square (Fig. 17(b)), and then back to a circle (Fig. 17(c)). For the cluster with 1052 atoms, the crater's top view evolves from a circle (Fig. 18(a)) to a square (Fig. 18(b)) which is rotated about 45° from that in Fig. 17(b). In an impact process, damage first spreads out in an isotropic manner and leads to a circular top view of the crater. Then the disordered atoms prefer to propagate along the four directions illustrated in Fig. 16(A). Since the region of displaced atoms is small, actually four small planes propagate along the four directions. The deformation rate along the intersection lines is higher, changing the crater's top view from a circle to a square, as shown in Fig. 17(b). In the late stage of impact, there is not enough energy to drive the small planes in Fig. 16(B) outward and the protrusion of the central parts gradually changes the

crater to a circular top view (Fig. 17(c)). Because the anisotropy is not evident for the cluster with 1052 atoms, the crater's top view keeps a circle until stacking faults burst (Fig. 15(c–f)), which makes damage to propagate along the four close packed planes {111}. The deformation rate in their intersection directions is larger (illustrated in Fig. 16(C)) and the top view of the crater evolves from a circle to a square rotated 45° (Fig. 18(b)). The same configuration persists at 10 ps as shown in Fig. 18(c).

It can be seen that energetic cluster impacts differ from nanoindentation in several aspects. Nanoindentation of MD simulations [38,39] aims to mimic quasi-equilibrium experiments, while the process of high energy cluster impacts is far away from the equilibrium state, characterized with high deformation rates. The impact case is intrinsically thermo-mechanically coupled and proceeds with possible state changes. The propagations of shock waves [15] as well as the front of the disordered atoms dominate the initial stage of the impact. The formation of the stacking faults and dislocation bursts, as frequently observed in the initial stage of nanoindention [38,39], only occurs in the late stage of cluster impact. The behavior of incipient plasticity also depends on the impact speed.

For the purposes of comparison, impacts of Si clusters on Si surface are also simulated. We adopt the potential
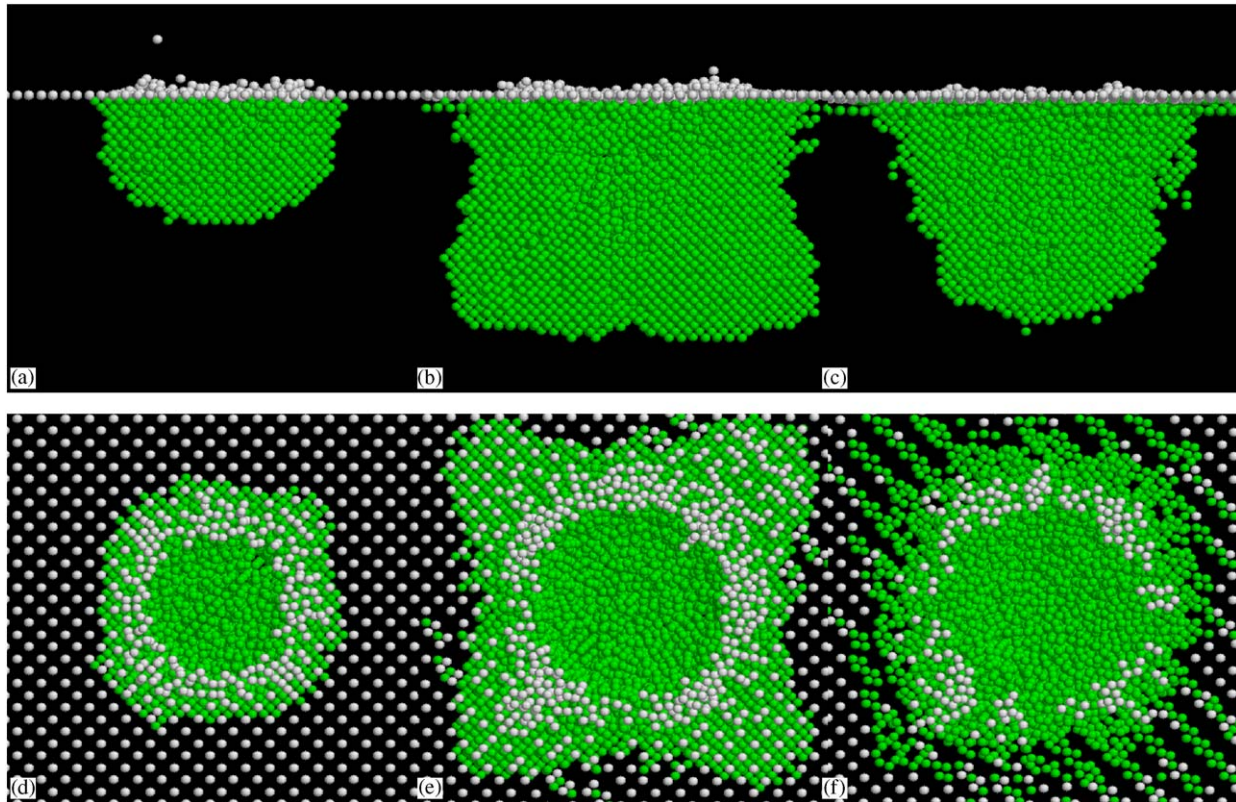
Fig. 19. (a)–(c) are frontal views of the local crystalline orders at 0.4, 1.3, and 2.5 ps after a Si cluster impacting on a Si substrate. The Si cluster contains 260 atoms. Graphs (d–f) correspond to the top view of graphs (a–c). The white spheres represent surface atoms, and the green ones represent atoms with none four-coordinated combinations.

proposed in Ref. [30]. The potential combines the Stillinger and Weber (SW) formulation [40] and the EAM form [26]. That potential provides a reasonable description of the energetics for all atomic coordinations Z, from the dimmer ($Z = 1$) to FCC and HCP ($Z = 12$). It accurately predicts formation energies and geometries of interstitial complexes: small clusters, interstitial-chain and planar {311} defects. One possible drawback of the potential is that the domain of the functions which comprise the potential is set by the extent of the fitting data. When evaluation of the potential leads to arguments beyond their domain, one has to use extrapolations. We regard that as a minor deficiency and ignorable for the purpose of qualitative comparison. Various graphs in Fig. 19 are snapshots of frontal and top views of local crystalline orders for a Si–Si cluster impact. It can be seen that the target first deforms in an isotropic manner in the initial stage of impact, as shown in Fig. 19(a, d). Anisotropic damage in the target emerges subsequently, as indicated in Fig. 19(b, e). More damage occurs in [1 1 0] and [1 $\bar{1}$ 0] directions, which is quite distinct from that of a Cu–Cu cluster impact. At the late stage of impact, the target recovers to an almost isotropic profile (Fig. 19(c, f)), in contrast to the anisotropic profile for the Cu–Cu impact (Fig. 15(c–f)).

For hypervelocity impacts of macroscopic bodies, the crater is almost hemispherical with volume proportional to

the impacting energy of the macrocluster, provided the impacting velocity is high enough [41]. This volume dependence on the impacting energy is valid for microcluster impacts at least for the following three cases. Case one is the simulated impacts of an Ar cluster (containing atoms from 13 to 3000) on a Si (0 0 1) surface [10], for total cluster energies of 0.5–55 keV. Case two is the simulated impacts of an Ar cluster (containing atoms from 200 to 800) on a Cu (0 0 1) surface [42], for total cluster energies of 6–20 keV. Case three is an experiment result featuring impacts of an Ar cluster (containing 3000 atoms) on a Au (1 1 1) surface [42], for total cluster energies between 20 and 150 keV. These cases indicate that the peculiar damage formation process is caused by an isotropic energy transportation process [10]. Here in our simulations the total Cu cluster energies vary from 0.5 to 35 keV and the total Si cluster energy is 4 keV. The simulation results here show that the damage formation process, created by a cluster impact, possesses certain anisotropy which is in accordance with the results developed by Nordiek et al. [43]. They found that the shape and size of craters depended on the surface orientation. They explain this anisotropy from two aspects. One is that the propagation velocity of disturbances relies on different crystallographic directions. The other is that the shear mode, a stretch along the [1 0 0] axis and a compression of the same amount

along the [0 1 0] axis, costs the lowest energy. Thus the crater formation is enhanced in directions $\langle 1\,0\,0 \rangle$ (Fig. 18(b)). Since dislocations manifests macroscopically as shear deformation, the burst of stacking faults (Fig. 18(b)) is the underlying cause of the enhanced deformation in directions $\langle 1\,0\,0 \rangle$. So the anisotropy of crystals dictates the anisotropic evolution of craters under the energetic cluster impacts. The displaced atoms propagate along preferable paths. Accordingly, the energy transportation process, characterized with multi-interactions among the cluster and surface atoms, is not an isotropic process. The underlying anisotropic lattice structure plays an important role in the impacting process and makes this transportation process anisotropic. For Cu cluster impacts on Cu surface, displaced atoms prefer to propagate along the intersection directions of slip places.

4. Conclusions and discussions

A seamless MPM/MD handshaking scheme is developed here. Modified interpolation shape functions are used to suppress artificial forces in MPM. Tests have demonstrated the satisfactory performance of this multiscale method in both dynamic and static simulations. The method is applicable to potentials including pair, triple or many-body interactions. Using this MPM/MD handshaking method, we have studied high energy Cu–Cu and Si–Si cluster impacts. The underlying lattice structure is found to play an important role in the deformation process. For Cu–Cu impacts, we observe that disordered atoms first spread isotropically, then propagate preferably in the intersection directions of slip planes {1 1 1}. For a larger cluster impact (such as a cluster with 1052 atoms), stacking faults burst in the later stage of impact. The evolution of craters validates this deformation process. For Si–Si impacts, the anisotropy is not evident comparing with that of Cu–Cu impacts, indicating the importance of underlying lattice structures. All simulations point to anisotropic damage formation.

In our simulation, the temperature is initialized at $0\,\mathrm{K}$, like that in Refs. [2,4,44]. For finite temperature simulations, velocity of material points should be thermalized to a Maxwellian distribution [44]. For different temperatures, elastic constants and lattice spacing vary in the MD region. Thus the elastic constants in the MPM region and lattice spacing in the handshaking region should change in accordance with that in the MD region. Another problem is the dissipation in the MPM region. If the elasticity theory is used in the MPM region, vibration modes will propagate undamped. In order to thermalize short-wavelength phonons and also to allow energy to be dissipated in the MPM region, the MPM degrees of freedom should be weakly coupled to a Brownian heat bath whose dynamics are set to the temperature at which the simulation is being performed [44]. Thus Newton's equations of motion are replaced by Langevin equation [45]. In this case, an external force, which combines a random force and a frictional dissipation term, is prescribed on each material point. Also a proper damping [24] is expected to reduce the reflection waves on the MPM/MD boundary.

References

[1] Kadau K, Germann TC, Lomdahl PS. International Journal of Modern Physics C 2004;15:193.

[2] Kohlhoff S, Gumbsch P, Fischmeister HF. Philosophical Magazine A 1991;64:851.

[3] Yang W, Tan HL, Guo TF. Modelling and Simulation in Materials Science and Engineering 1994;2:767.

[4] Abraham FF, Broughton JQ, Bernstein N, Kaxiras E. Computers in Physics 1998;12:538.

[5] Tan HL, Yang W. Acta Mechanica Sinica 1994;10:237.

[6] Tadmor EB, Ortiz M, Phillips R. Philosophical Magazine A 1996;73:1529.

[7] Shenoy VB, Miller R, Tadmor EB, Rodney D, Phillips R, Ortiz M. Journal of Mechanics and Physics of Solids 1999;47:611.

[8] Yamada I, Matsuo J, Insepov Z, Aoki T, Seki T, Toyoda N. Nuclear Instruments and Methods B 2000;164-165:944.

[9] Haberland H, Insepov Z, Moseler M. Physical Review B 1995;51:11061.

[10] Aoki T, Matsuo J, Insepov Z, Yamada I. Nuclear Instruments and Methods B 1997;121:49.

[11] Aoki T, Seki T, Matsuo J, Insepov Z, Yamada I. Nuclear Instruments and Methods B 1999;153:264.

[12] Aoki T, Matsuo J, Takaoka G. Nuclear Instruments and Methods B 2003;202:278.

[13] Insepov Z, Yamada I. Nuclear Instruments and Methods B 1999;153:199.

[14] Insepov Z, Yamada I. Nuclear Instruments and Methods B 1996;112:16.

[15] Ma XL, Yang W. Nanotechnology 2004;15:449.

[16] Tillotson JH. General Atomic Division of General Dynamics Report GA-3216, 1962.

[17] Mishin Y, Mehl MJ, Papaconstantopoulos DA, Voter AF, Kress JD. Physical Review B 2001;63:224106.

[18] Sulsky D, Chen Z, Schreyer HL. Computer Methods in Applied Mechanics and Engineering 1994;118:179.

[19] Burgess D, Sulsky D, Brackbill JU. Journal of Computational Physics 1992;103:1.

[20] Tan HL, Nairn JA. Computer Methods in Applied Mechanics and Engineering 2002;191:2095.

[21] Sulsky D, Zhou SJ, Schreyer HL. Computer Physics Communications 1995;87:236.

[22] Bardenhagen SG. Journal of Computational Physics 2002;180:383.

[23] Hughes T. The finite element method. Upper Saddle River, NJ: Prentice Hall; 1987.

[24] Moseler M, Nordiek J, Haberland H. Physical Review B 1997;56:15439.

[25] Bardenhagen SG, Kober EM. CMES-Computer Modeling in Engineering and Sciences 2004;5:477.

[26] Daw MS, Baskes MI. Physical Review B 1984;29:6443; Daw MS, Baskes MI. Physical Review Letters 1983;50:1285.

[27] Sulsky D, Brackbill JU. Journal of Computational Physics 1991; 96:339.

[28] Doyama M, Kogure Y. Computational Materials Sciences 1999;14:80.
[29] Schiøtz J, Vegge T, Di Tolla FD, Jacobsen KW. Physical Review B 1999;60:11971.
[30] Lenosky TJ, et al. Modelling and Simulation in Materials Science and Engineering 2000;8:825.
[31] DePriesto AE, Metiu H. Journal of Chemical Physics 1989;90:1229.
[32] Mitchell AC, Nellis WJ. Journal of Applied Physics 1981;52:3363; Mitchell, et al. Journal of Applied Physics 1991;69:2981.
[33] Mao HK, Bell PN, Shaner JW, Steinberg DJ. Journal of Applied Physics 1978;49:3276.
[34] Wang Y, Chen DQ, Zhang XW. Physical Review Letters 2000; 84:3220.
[35] Nellis, et al. Physical Review Letters 1988;60:1414.
[36] Caturla MJ, Diaz de la Rubia T, Gilmer GH. Nuclear Instruments and Methods B 1995;106:1.
[37] Swygenhoven HV, Farkas D, Caro A. Physical Review B 2000; 62:831.
[38] Ma XL, Yang W. Nanotechnology 2003;14:1208.
[39] Kelchner CL, Plimpton SJ, Hamilton JC. Physical Review B 1998; 58:11085;
Li J, Van Vliet K, Zhu T, Yip S, Suresh S. Nature 2002;418:307;
Zhu T, Li J, Van Vliet KJ, Ogata S, Yip S, Suresh S. Journal of the Mechanics and Physics of Solids 2004;52:691.
[40] Stillinger F, Weber T. Physical Review B 1985;31:5262.
[41] Herrmann W, Wilbeck JS. International Journal of Impact Engineering 1987;5:307.
[42] Insepov Z, Yamada I. Nuclear Instruments and Methods B 1999;153:199.
[43] Nordiek J, Moseler M, Haberland H. Radiation Effects and Defects in Solids 1997;142:27.
[44] Broughton JQ, Abraham FF, Bernstein N, Kaxiras E. Physical Review B 1999;60:2391.
[45] Adelmann SA, Doll JD. Journal of Chemical Physics 1976;64:2375; Adelmann SA, Doll JD. Journal of Chemical Physics 1987;86:4885.